ChemComm

COMMUNICATION

Check for updates

Fine tuning of intra-lattice electron transfers through site doping in tetraoxolene-bridged iron honeycomb layers†

Yoshihiro Sekine, [iD] ab Jian Chen, a Naoki Eguchi [iD] b and Hitoshi Miyasaka [iD] *ab

The precise control of intra-lattice multiple electron transfers was demonstrated in the solvated and desolvated species of the tetraoxolene-bridged Fe honeycomb layer system, $(NPr_4)_2[Fe_2(Cl_2An)_3]\cdot$ (solv) (Cl_2An^{n-} = 2,5-dichloro-3,6-dihydroxy-1,4-benzoquinonate; NPr_4^+ = tetrapropylammonium cation), by the site-doping of the Cl_2An^{n-} bridging unit using X_2An^{n-} units with X = Br or F.

Exploring new stimuli-controllable functional systems is important in the field of materials science.[1–4] These systems can be obtained by achieving thermally driven electron transfers (TDETs) in a material,[5] which can successfully induce a state (or phase) change in materials at a transition temperature ($T_{1/2}$). Moreover, modifications of the physical properties of materials such as electronic conductivity,[6] magnetic properties,[7] elasticity,[8] and the dielectric property can be attained.[9] Currently, the relevant systems in the charge-transfer metal complexes, which are composed of electron-donor (D) and -acceptor (A) moieties,[9–20] and organic charge transfer systems,[21–24] have been investigated. Nevertheless, the systematic fine tuning of the variable charge states is still challenging; however, it can potentially be used for the application of these systems in molecular devices and sensors.[1–3]

Recently, we have reported two kinds of tetraoxolene-bridged iron honeycomb layered compounds, $(NPr_4)_2[Fe_2(Cl_2An)_3]\cdot2(acetone)\cdot H_2O$ (**0**; Cl_2An^{n-} = 2,5-dichloro-3,6-dihydroxy-1,4-benzoquinonate; NPr_4^+ = tetrapropylammonium cation)[15] and their desolvated compound $(NPr_4)_2[Fe_2(Cl_2An)_3]$ (**0-d**).[16] The former exhibited a TDET at $T_{1/2a}$ = 236 K between the phases of $[Fe^{III}_2(Cl_2An^{2-})(Cl_2An^{\bullet 3-})_2]^{2-}$ at $T < T_{1/2a}$ and

$[Fe^{II}Fe^{III}(Cl_2An^{2-})_2(Cl_2\text{-}An^{\bullet 3-})]^{2-}$ at $T > T_{1/2a}$,[15] while the latter underwent a stepwise TDET at $T_{1/2b}$ = 317 K and $T_{1/2c}$ = 354 K which changed phases from $[Fe^{III}_2(Cl_2An^{2-})(Cl_2An^{\bullet 3-})_2]^{2-}$ at $T < T_{1/2b}$ to $[Fe^{II}_2(Cl_2An^{2-})_3]^{2-}$ at $T > T_{1/2c}$ via the intermediate state of $[Fe^{II}Fe^{III}(Cl_2An^{2-})_2(Cl_2An^{\bullet 3-})]^{2-}$ at $T_{1/2b} < T < T_{1/2c}$ (Scheme 1a).[16] In addition, compounds **0** and **0-d** are reversible via the solvation and desolvation processes, respectively. Hence, the systematic and continuous tuning of these phases were favorable due to being unprecedented in multiple TDET systems.

Herein, we report a precise tuning of the multiple transition temperatures $T_{1/2a}$, $T_{1/2b}$, and $T_{1/2c}$ based on a chemical technique of site-doping for the charge-transfer materials **0** and **0-d**. A rational incorporation of the redox metal ions and bridging

a Institute for Materials Research, Tohoku University, 2-1-1 Katahira, Aoba-ku, Sendai 980-8577, Japan. E-mail: miyasaka@imr.tohoku.ac.jp;
Fax: +81-22-215-2031; Tel: +81-22-215-2030

b Department of Chemistry, Graduate School of Science, Tohoku University, 6-3 Aramaki-Aza-Aoba, Aoba-ku, Sendai 980-8578, Japan
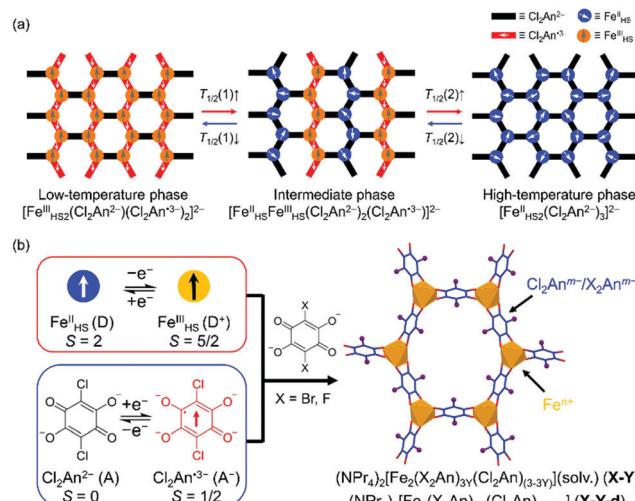
Scheme 1 Schematic representations of the investigated tetraoxolene-bridged Fe honeycomb layers. (a) The variations of charge-ordered states in **0** and **0-d**, where for **0**, $T_{1/2}(1)$ was $T_{1/2a}$ (i.e., there was no high-temperature phase for **0**), and for **0-d**, $T_{1/2}(1)$ and $T_{1/2}(2)$ correspond to $T_{1/2b}$ and $T_{1/2c}$, respectively. (b) Schematic route for the syntheses of site-doped solid solution compounds in this work.

ligands into the charge-transfer skeleton is one of the efficient strategies in achieving the fine tuning of TDET.[17,18,25–28] In this work, the Cl_2An^{m-} unit in $\mathbf{0}$ and $\mathbf{0}$-d was replaced by X_2An^{m-} with X = F or Br in several ratios in the isostructural series where F_2An^{m-} = 2,5-difluoro-3,6-dihydroxy-1,4-benzoquinonate and Br_2An^{m-} = 2,5-dibromo-3,6-dihydroxy-1,4-benzoquinonate. Because the F_2An^{2-} and Br_2An^{2-} units act as stronger and weaker electron acceptors than Cl_2An^{2-}, respectively, their solid-solution series revealed inverse trends in the doping rate dependence of $T_{1/2}$s between the F-doped and Br-doped series, that is, proportional and inversely-proportional, respectively, despite being linearly variable in both cases.

The solvated compound series of the solid solutions $(NPr_4)_2[Fe_2(Cl_2An)_{(3-3Y)}(X_2An)_{3Y}]\cdot2(acetone)\cdot H_2O$ (**X-Y**) as X = Br with Y = 0.10 (**Br-0.10**), 0.18 (**Br-0.18**), 0.35 (**Br-0.35**), 0.65 (**Br-0.65**) and X = F with Y = 0.06 (**F-0.06**), 0.12 (**F-0.12**), 0.17 (**F-0.17**), 0.24 (**F-0.24**), 0.31 (**F-0.31**), 0.42 (**F-0.42**) were synthesized using an identical procedure for $\mathbf{0}$. Specifically, H_2Br_2An or H_2F_2An was mixed into an H_2Cl_2An solution in various ratios (Scheme 1b),[15] where the Y value was obtained from the halogen elemental analyses for the **X-Y** and their desolvated series, **X-Y-d** (ESI†). The Y doping ratio was approximately identical to the mixing ratio in the synthetic procedures.

All compounds of the solvated form (**X-Y**) were isostructural to $\mathbf{0}$ in the Y-doped region of $0.65 \geq Y$ and $0.42 \geq Y$ for X = Br and F, respectively. The compounds crystalized in the monoclinic $P2_1/c$ space group with an asymmetric unit containing two crystallographically independent Fe^{n+} ions, three Cl_2An^{m-}/X_2An^{m-} ligands, and two NPr_4^+ cations (Fig. S1 and Table S1, S2, ESI†). The Fe ions and Cl_2An/X_2An ligands formed a honeycomb anionic layer $[Fe_2(Cl_2An/X_2An)_3]^{2-}$ in the (100) plane. The occupancy ratio (*i.e.*, the X/Cl ratios) in the Cl_2An/X_2An ligands was fixed using the ratio obtained using the halogen elemental analyses (ESI†). The polycrystalline samples of the **X-Y** series were macroscopically evaluated using the powder X-ray diffractograms (PXRD) recorded at room temperature and compared with the simulated patterns determined using the single crystal XRD (SC-XRD) analyses (Fig. 1). We investigated the highly doped compounds beyond the doping rate of $0.65 < Y$ and $0.42 < Y$ for X = Br and F, respectively. The polycrystalline samples for the highly doped compounds and X_2An^{m-}-pure compounds had different PXRD patterns from that of $\mathbf{0}$. Unfortunately, the SC-XRD analyses for the highly doped samples did not succeed because of their low quality single crystals.

The desolvated series **X-Y-d** were obtained by using the samples of **X-Y**; $(NPr_4)_2[Fe_2(Cl_2An)_{(3-3Y)}(X_2An)_{3Y}]$ (X = Br; **Br-0.10-d** for Y = 0.10, **Br-0.18-d** for Y = 0.18, **Br-0.35-d** for Y = 0.35, **Br-0.65-d** for Y = 0.65, X = F; **F-0.06-d** for Y = 0.06, **F-0.12-d** for Y = 0.12, **F-0.17-d** for Y = 0.17, **F-0.24-d** for Y = 0.24, **F-0.31-d** for Y = 0.31, **F-0.42-d** for Y = 0.42) (Scheme 1b, Fig. S2, ESI†). The SC-XRD analysis at 103 K revealed that the **X-Y-d** compounds successfully changed to an isostructural 2D honeycomb layer structure with $\mathbf{0}$-d (Fig. S3, S4 and Tables S3, S4, ESI†). Both the **Br-Y-d** and **F-Y-d** were crystallized in the monoclinic space group, $P2_1/n$, with an asymmetric unit containing one
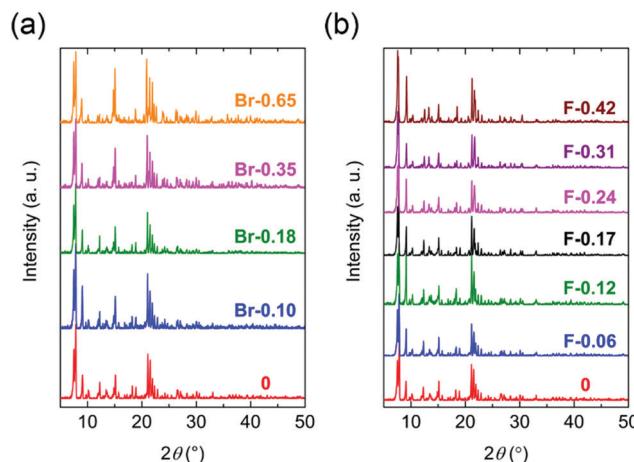
Fig. 1 PXRD patterns of **Br-Y** (a) and **F-Y** (b) measured at room temperature.

crystallographically unique Fe^{n+} (Fe × 1), one and a half Cl_2An^{m-}/X_2An^{m-} ligands, and one NPr_4^+ cation (Fig. S3, ESI†) NPr_4^+ was located between the honeycomb anionic layers $[Fe_2(Cl_2An/X_2An)_3]^{2-}$ formed by the Fe ions and Cl_2An^{m-}/X_2An^{m-} ligands, which were parallel to the (10–1) plane (Fig. S3, ESI†).

The oxidation states of the Fe^{n+} and X_2An^{m-} ligands for the series of **X-Y** and **X-Y-d** at 103 K were estimated from the local bond lengths of Fe–O and C–O in the Cl_2An^{m-}/X_2An^{m-} because their bond distances characteristically changed depending on their oxidation states.[15,16,19,29] At 103 K, the electronic states of all the site-doped compounds were estimated to be a low-temperature state, which was similarly observed in $\mathbf{0}$ and $\mathbf{0}$-d as $([(Fe^{III})_2(Cl_2An^{2-})(Cl_2An^{\bullet3-})_2]^{2-})$ (see the ESI†).

The temperature dependence of the magnetic susceptibilities ($\chi = M/H$) of **Br-Y** (Y = 0.10, 0.18, 0.35, 0.65) and **F-Y** (Y = 0.06, 0.12, 0.17, 0.24, 0.31, 0.42) was measured by applying a 1 kOe dc field (H_{dc}) in the temperature range of 300 to 1.8 K (Fig. 2a and 3a and Fig. S5 and S6, ESI†). The $\chi_m T$ values at 300 K were in the range of 9.72–10.07 cm^3 K mol^{-1} and 9.89–11.28 cm^3 K mol^{-1} for the series of **Br-Y** and **F-Y**, respectively, which were varied in a narrow range (Table S5, ESI†). However, it is difficult to conclude that the variation of $\chi_m T$ values at 300 K was caused by the electronic state modulations in the series because of the presence of a strong antiferromagnetic spin coupling between the Fe^{III} with S = 5/2 and $X_2An^{\bullet3-}$ with S = 1/2 (Fig. S5, S6 and Table S5, ESI†).[15,16,29–32] As the original $\mathbf{0}$ compound showed abrupt increases of χ_m and $\chi_m T$ at $T_{1/2a}$ = 236 K upon cooling concomitant with the one-step transition from the intermediate phase of $[Fe^{II}Fe^{III}(Cl_2An^{2-})_2(Cl_2An^{\bullet3-})]^{2-}$ to a low temperature phase of $[Fe^{III}_2(Cl_2An^{2-})(Cl_2An^{\bullet3-})_2]^{2-}$, all doped **X-Y** compounds exhibited similar transition features in χ_m and $\chi_m T$. However, their $T_{1/2a}$ shifted to lower and higher temperatures with increasing doping rate Y for **Br-Y** and **F-Y**, respectively, compared with $T_{1/2a}$ = 236 K for $\mathbf{0}$ (Fig. 2a and 3a); the $T_{1/2a}$ values reached 184 K (Δ51 K from $T_{1/2a}$ in $\mathbf{0}$) and 270 K (Δ34 K) for **Br-0.65** and **F-0.31**, respectively. Specifically, $T_{1/2a}$s in both **Br-Y** and **F-Y** linearly varied whereas the doping rate of
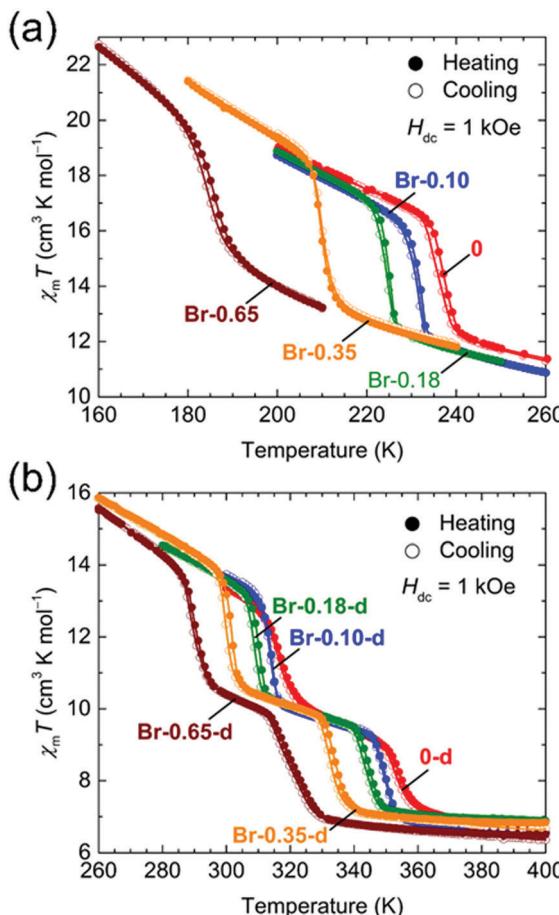
Fig. 2 Temperature dependence of $\chi_m T$ for **Br-Y** (a) and **Br-Y-d** (b) measured at $H_{dc} = 1$ kOe ($\chi_m = M_m/H_{dc}$), where the narrow temperature ranges of 160–260 K and 260–400 K, respectively, were used.

Fig. 3 Temperature dependence of $\chi_m T$ for **F-Y** (a) and **F-Y-d** (b) measured at $H_{dc} = 1$ kOe ($\chi_m = M_m/H_{dc}$), where narrow temperature ranges of 220–300 K and 300–400 K, respectively, were used.

Y had inversely proportional and proportional trends on Y, respectively (Fig. 4 and Fig. S7, ESI†), where the $T_{1/2a}$ temperatures were determined from the peak in the $d\chi_m T/dT$ vs. T plots and their error bars were estimated from the half-value width of the peaks (Fig. S8, ESI†). The slopes of the $T_{1/2a}$ variations were -77.3 and 110.3 K Y^{-1} for **Br-Y** and **F-Y**, respectively. The **F-Y** series tended to have larger error bars with increasing Y than that of the **Br-Y** series, and $T_{1/2a}$ was not assigned in **F-0.42**, which could be due to the large random domain effect of **F-X**. Nevertheless, these trends of $T_{1/2a}$ in **Br-Y** and **F-Y** could be due to the site-doping of X_2An^{m-} with different electron acceptabilities, that is, $F_2An^{2-} > Cl_2An^{2-} > Br_2An^{2-}$ (electronegativity of halogen atom: $F > Cl > Br$).[33,34] The magnetic profile in the entire temperature range from 300 to 1.8 K was similar to that for **0** excluding $T_{1/2a}$; however, the magnetic correlation lengths at low temperatures were slightly different from each other. **Br-Y** had a tendency to have a longer correlation length in highly doped compounds, whereas it was approximately inversed for **F-Y** (Fig. S5 and S6, ESI†). Furthermore, the superparamagnetic behavior of single-chain magnets was observed at lower temperatures as shown in the original compound **0** (Fig. S9, ESI†), which can be attributed to the ferrimagnetic chain motif of $[-Fe^{III}-(Cl_2An^{\bullet 3-}/X_2An^{\bullet 3-})-]$ ($S_{Fe} = 5/2$, $S_{rad} = 1/2$) separated by

the diamagnetic Cl_2An^{2-}/X_2An^{2-} bridges in the honeycomb layer (low-temperature phase in Scheme 1a).[15]

The temperature dependence of the magnetic susceptibility for the doped series of the desolvated compounds **X-Y-d** was measured in the temperature range of 400–1.8 K. As the χ_m–and $\chi_m T - T$ plots for **0-d** showed a two-step transition (abrupt increasing of χ_m and $\chi_m T$ upon cooling) at $T_{1/2b} = 316$ K and $T_{1/2c} = 353$ K, corresponding to the variation of the electronic state from $[Fe^{II}_2(Cl_2An^{2-})_3]^{2-}$ at $T > T_{1/2c}$ to $[Fe^{III}_2(Cl_2An^{2-})(Cl_2An^{\bullet 3-})_2]^{2-}$ at $T < T_{1/2b}$ via an intermediate state of $[Fe^{II}Fe^{III}(Cl_2An^{2-})_2(Cl_2-An^{\bullet 3-})]^{2-}$ at $T_{1/2b} < T < T_{1/2c}$ (Scheme 1a),[16] the site-doped **X-Y-d** series showed similar two-step transitions. The error bar was larger in the highly doped species in **F-X-d** (Fig. 2b and 3b), owing to the characteristic domain effect. Moreover, the transition temperatures of $T_{1/2b}$ and $T_{1/2c}$ in **Br-Y-d** clearly shifted linearly to lower temperatures. On the other hand, the tendency in **F-Y-d** was slightly different from that of **F-Y**. The transition temperature of $T_{1/2c}$ in **F-Y-d** tended to shift to higher temperatures in the solid solution species with lower doping rates; however, $T_{1/2b}$ was approximately constant in the series. As mentioned above, the domain effect was characteristic in the series of **F-Y-d** and **F-Y**.
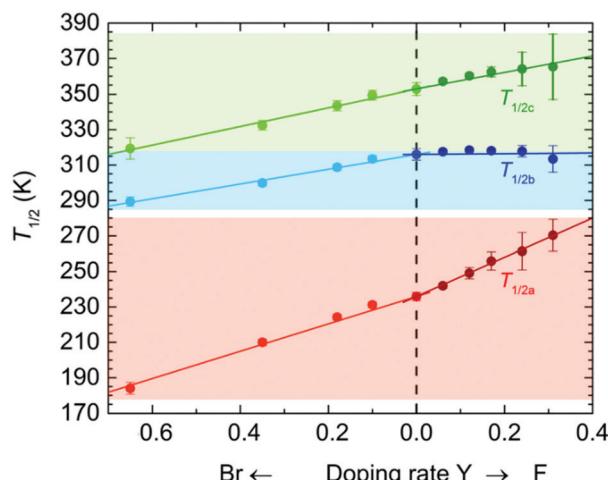
Fig. 4 Variations of the $T_{1/2}$ value of TDETs for the site-doped rate Y in the solid solution series of **X-Y** and **X-Y-d**, whereas the basis of $Y = 0$ corresponded to **0** and **0-d**. The left and right scales represent **Br-Y/Br-Y-d** and **F-Y/F-Y-d**, respectively. The solid lines are least-square linear fitting lines for the respective series.

Hence, it is difficult to conclude that $T_{1/2b}$ was not affected by the site-doping of F_2An^{m-}. Although there was no clear reason, the transition temperatures in **F-Y-d** were slightly affected by the doping of the site-doping of F_2An^{m-}. The slope of the $T_{1/2b}$ and $T_{1/2c}$ variations *versus* Y was −41.7 and −52.7 K Y^{-1} for **Br-Y-d** and 2.0 and 46.5 K Y^{-1} and **F-Y-d** (Fig. S7, ESI†). The difference in tendencies can be explained by the electron-acceptability of $F_2An^{2-} > Cl_2An^{2-} > Br_2An^{2-}$.

The site-doping of F_2An^{m-} influenced the magnetic phase of the solid-solution materials of **F-Y-d**. The **F-Y-d** species with $Y \leq 0.24$ have a maximum of χ_m at approximately 23 K followed by a steep decrease after further cooling. This was indicative of an antiferromagnetic ground state as similarly found in **0-d** and **Br-Y-d** (Fig. S5, ESI†); however, the decrease of χ_m did not occur in the cases with higher doping rate. Instead, the superparamagnetic behavior of single-chain magnets was observed in the low-temperature phase of **F-Y-d** with $0.24 < Y$ (Scheme 1a).

In summary, we succeeded in the precise tuning of multiple TDET at three $T_{1/2}$s transition temperatures through the chemical-site doping of two types of tetraoxolene-bridged Fe-based honeycomb layer compounds. This provided an "on-demand TDET" in a temperature range of 184 to 365 K.

Conflicts of interest

There are no conflicts to declare.

Notes and references

1 O. Sato, *Nat. Chem.*, 2016, **8**, 644–656.
2 M. E. Guillermo and E. Coronado, *Chem. Soc. Rev.*, 2018, **47**, 533–557.
3 A. Dei, D. Gatteschi, C. Sangregorio and L. Sorace, *Acc. Chem. Res.*, 2004, **37**, 827–835.
4 E. Coronado, *Nat. Rev. Mater.*, 2019, **5**, 87–104.
5 J. S. Miller and K. S. Min, *Angew. Chem., Int. Ed.*, 2009, **48**, 262–272.
6 M. Mitsumi, T. Nishitani, S. Yamasaki, N. Shimada, Y. Komatsu, K. Toriumi, Y. Kitagawa, M. Okumura, Y. Miyazaki, N. Córska, A. Inaba, A. Kanda and N. Hanasaki, *J. Am. Chem. Soc.*, 2014, **136**, 7026–7037.
7 M. Nihei, Y. Sekine, N. Suganami, K. Nakazawa, A. Nakano, H. Nakano, Y. Murakami and H. Oshio, *J. Am. Chem. Soc.*, 2011, **133**, 3592–3600.
8 K. Boukheddaden, E. D. Loutete-Dangui, E. Codjovi, M. Castro, J. A. Rodriguéz-Velamazán, S. Ohkoshi, H. Tokoro, M. Koubaa, Y. Abid and F. Varret, *J. Appl. Phys.*, 2011, **109**, 013520.
9 N. Hoshino, F. Iijima, G. N. Newton, N. Yoshida, T. Shiga, H. Nojiri, A. Nakao, R. Kumai, Y. Murakami and H. Oshio, *Nat. Chem.*, 2012, **4**, 921–926.
10 R. M. Buchanan and C. G. Pierpont, *J. Am. Chem. Soc.*, 1980, **102**, 4951–4957.
11 D. F. Li, R. Clérac, O. Roubeau, E. Harté, C. Mathonière, R. L. Bris and S. M. Holmes, *J. Am. Chem. Soc.*, 2008, **130**, 252–258.
12 D. Kiriya, H. C. Chang and S. Kitagawa, *J. Am. Chem. Soc.*, 2008, **130**, 5515–5522.
13 H. Miyasaka, N. Motokawa, T. Chiyo, M. Takemura, M. Yamashita, H. Sagayama and T. Arima, *J. Am. Chem. Soc.*, 2011, **133**, 5338–5345.
14 M. Nihei, Y. Okamoto, Y. Sekine, N. Hoshino, T. Shiga, I. P. C. Liu and H. Oshio, *Angew. Chem., Int. Ed.*, 2012, **51**, 6361–6364.
15 J. Chen, Y. Sekine, Y. Komatsumaru, S. Hayami and H. Miyasaka, *Angew. Chem., Int. Ed.*, 2018, **57**, 12043–12047.
16 J. Chen, Y. Sekine, A. Okazawa, H. Sato, W. Kosaka and H. Miyasaka, *Chem. Sci.*, 2020, **11**, 3610–3618.
17 K. Nakabayashi and H. Miyasaka, *Chem. – Eur. J.*, 2014, **20**, 5121–5131.
18 K. Nakabayashi, M. Nishio and H. Miyasaka, *Inorg. Chem.*, 2016, **55**, 2473–2480.
19 J. A. DeGayner, K. Y. Wang and T. D. Harris, *J. Am. Chem. Soc.*, 2018, **140**, 6550–6553.
20 W. Kosaka, Y. Takahashi, M. Nishio, K. Narushima, H. Fukunaga and H. Miyasaka, *Adv. Sci.*, 2018, **5**, 1700526.
21 J. B. Torrance, A. Girlando, J. J. Mayerle, J. I. Crowley, V. Y. Lee and P. Batail, *Phys. Rev. Lett.*, 1981, **47**, 1747–1750.
22 S. Horiuchi, R. Kumai, Y. Okimoto and Y. Tokura, *Chem. Phys.*, 2006, **325**, 78–91.
23 S. Horiuchi, R. Kumai, Y. Okimoto and Y. Tokura, *Phys. Rev. B: Condens. Matter Mater. Phys.*, 1999, **59**, 11267–11275.
24 G. Saito and Y. Yoshida, *Bull. Chem. Soc. Jpn.*, 2007, **80**, 1–137.
25 M.-H. Zeng, B. Wang, X.-Y. Wang, W.-X. Zhang, X.-M. Chen and S. Gao, *Inorg. Chem.*, 2006, **45**, 7069–7076.
26 M. Nishio, N. Hoshino, W. Kosaka, T. Akutagawa and H. Miyasaka, *J. Am. Chem. Soc.*, 2013, **135**, 17715–17718.
27 S. Chorazy, J. J. Stanek, W. Nogas, A. M. Majcher, M. Rams, M. Kozieł, E. Juszyńska-Gałązka, K. Nakabayashi, S.-I. Ohkoshi, B. Sieklucka and R. Podgajny, *J. Am. Chem. Soc.*, 2016, **138**, 1635–1646.
28 L. Liu, L. Li, M. E. Ziebel and T. D. Harris, *J. Am. Chem. Soc.*, 2020, **142**, 4705–4713.
29 J. A. DeGayner, I. R. Jeon, L. Sun, M. Dincă and T. D. Harris, *J. Am. Chem. Soc.*, 2017, **139**, 4175–4184.
30 A. Dei, D. Gatteschi, L. Pardi and U. Russo, *Inorg. Chem.*, 1991, **30**, 2589–2594.
31 I. R. Jeon, B. Negru, R. P. Van Duyne and T. D. Harris, *J. Am. Chem. Soc.*, 2015, **137**, 15699–15702.
32 S. A. Sahadevan, A. Abhervé, N. Monni, D. P. Sáenz, J. R. Galán-Mascarós, J. C. Waerenborgh, B. J. C. Vieira, P. Auban-Senzier, S. Pillet, E. Bendeif, P. Alemany, E. Canadell, M. L. Mercuri and N. Avarvari, *J. Am. Chem. Soc.*, 2018, **140**, 12611–12621.
33 M. Atzori, S. Benmansour, G. Mínguez Espallargas, M. Clemente-León, A. Abhervé, P. Gómez-Claramunt, E. Coronado, F. Artizzu, E. Sessini, P. Deplano, A. Serpe, M. L. Mercuri and C. J. Gómez-García, *Inorg. Chem.*, 2013, **52**, 10031–10040.
34 R. Murase, B. F. Abrahams, D. M. D'Alessandro, C. G. Davies, T. A. Hudson, G. N. L. Jameson, B. Moubaraki, K. S. Murray, R. Robson and A. L. Sutton, *Inorg. Chem.*, 2017, **56**, 9025–9035.